

# In Situ X-ray Microtomography of Stress Corrosion Cracking and Corrosion Fatigue in Aluminum Alloys

SUDHANSHU S. SINGH,<sup>1</sup> TYLER J. STANNARD,<sup>2</sup> XIANGHUI XIAO,<sup>3</sup> and NIKHILESH CHAWLA<sup>2,4</sup>

1.—Department of Materials Science and Engineering, Indian Institute of Technology Kanpur, Kanpur 208016, India. 2.—Materials Science and Engineering, Arizona State University, Tempe, AZ 85287-6106, USA. 3.—Advanced Photon Source, Argonne National Laboratory, Argonne, IL 60439, USA. 4.—e-mail: nchawla@asu.edu

Structural materials are subjected to combinations of stress and corrosive environments that work synergistically to cause premature failure. Therefore, studies on the combined effect of stress and corrosive environments on material behavior are required. Existing studies have been performed in two dimensions that are inadequate for full comprehension of the three-dimensional (3D) processes related to stress corrosion cracking (SCC) and corrosion-fatigue (CF) behavior. Recently, x-ray synchrotron tomography has evolved as an excellent technique to obtain the microstructure in 3D. Moreover, being nondestructive in nature, x-ray synchrotron tomography is well suited to study the evolution of microstructure with time (4D, or fourth dimension in time). This article presents our recent 4D studies on SCC and CF of Al 7075 alloys using x-ray synchrotron tomography.

## INTRODUCTION

In almost all applications, structural components are not only subjected to stress but also exposed to a corrosive environment. Therefore, the design and development of high-performance structural materials require a thorough understanding of how mechanical stresses, microstructure, and environment are related. For many decades, two-dimensional (2D) techniques were used to study the structure of materials. Yet, this approach is often inadequate as the properties in the bulk and on the surface have been found to be much different.<sup>1</sup> Several three-dimensional (3D) techniques have recently become available to visualize and quantify the microstructure in three dimensions.<sup>2</sup> Among them, x-ray tomography has gained popularity as it is nondestructive in nature and requires minimal sample preparation time.<sup>3,4</sup> As a result of improved optics and computation, the imaging resolution in x-ray synchrotron tomography has now reached submicrometer to nanometer range.<sup>5–10</sup>

In the last two decades, many *ex situ* x-ray tomography experiments have been conducted to understand the mechanical behavior of materials. Yet, these *ex situ* experiments have consisted of

postmortem characterization after testing. A complete understanding of the structure–property correlation requires a thorough understanding of the evolution of the microstructure with time (also called 4D studies, where the fourth dimension is time).<sup>11,12</sup> The nondestructive nature and high brilliance of x-ray synchrotron tomography make it suitable for *in situ* mechanical testing experiments, where microstructure evolution can be studied as a function of time under the applied load.<sup>13–15</sup> Many *in situ* experiments under compression,<sup>16,17</sup> tension,<sup>2,18,19</sup> creep,<sup>20</sup> and cyclic loading (fatigue)<sup>21–25</sup> have been conducted.

*In situ* x-ray synchrotron tomography experiments are of utmost importance in the investigation of stress corrosion cracking (SCC) and corrosion fatigue (CF), where higher temporal resolution is required. Nevertheless, conducting *in situ* experiments in corrosive media is extremely challenging, especially with regard to the mechanical testing stage design. The difficulties in designing the loading stage include specimen alignment, weight limitation, requirement of a material that is transparent to x-rays and sustains mechanical loading, and reaction of a corrosive environment with the parts of a loading stage. Over the years, several

in situ experiments have been conducted to investigate stress corrosion cracking (SCC)<sup>26–28</sup> and corrosion fatigue.<sup>29</sup> Babout et al.<sup>26</sup> and Marrow et al.<sup>27</sup> observed the development of bridging ligaments during propagation of stress corrosion cracks in stainless steel. They proposed that these bridges provide resistance to the propagation of stress corrosion cracks. Later, King et al.<sup>28</sup> coupled x-ray tomography with diffraction contrast tomography (DCT) to demonstrate that certain grain boundaries are resistant to IGSCC (intergranular stress corrosion cracking) and that these boundaries are also associated with crack bridging ligaments. These studies have been conducted in steels and do not quantify the stress corrosion crack growth rates. Moreover, studies on the effect of stress on localized corrosion behavior of inclusions and visualization/quantification of hydrogen bubbles evolution in Al alloys have not been performed.

In this article, we report our recent results on the use of x-ray synchrotron tomography to understand the SCC and corrosion-fatigue behavior of 7075 Al alloys. Details of the loading stages to perform in situ experiments in liquid and moisture environments have been provided. Three in situ examples have been used to demonstrate the importance and necessity of x-ray synchrotron tomography in the investigation of stress corrosion cracking and corrosion fatigue.

## EXPERIMENTAL SETUP

### Materials and X-ray Tomography

Stress corrosion cracking and corrosion-fatigue tests were performed on rolled 7075 aluminum alloys. These alloys are used in structural applications as a result of their high strength-to-weight ratio.<sup>30,31</sup> Al 7075 alloys contain second-phase particles, such as precipitates and inclusions.<sup>30,31</sup> These nanoscale precipitates hinder the movement of dislocations and therefore provide an excellent strength-to-weight ratio. Yet, the presence of the second-phase particles in these alloys can also increase their susceptibility to SCC and CF. The typical composition of rolled Al 7075 alloy used in the study was 5.63 Zn, 2.45 Mg, 1.55 Cu, 0.19 Cr, 0.18 Fe, 0.049 Ti, 0.045 Si, 0.008 Mn, 0.004 Ni, and rest Al (all in wt.%). The average values of the grain size of this alloy were  $\sim 50 \mu\text{m}$  along the S direction,  $\sim 300 \mu\text{m}$  along the T direction, and  $\sim 900 \mu\text{m}$  along the L direction. Figure 1a shows the schematic of a rolled plate indicating all directions and planes. In rolling technology, L represents the longitudinal or rolling direction, T represents the transverse direction, and S represents the short-transverse direction. In situ experiments were performed in commercially available peak-aged (T651) or under-aged conditions. To obtain an under-aged condition, 7075-T651 aluminum alloy was first solution treated at 475°C for 2 h, then quenched in water, and finally aged at 120°C for 80 min. The average

Vickers hardness values of T651 and under-aged tempers were  $\sim 176$  HV and  $\sim 136$  HV, respectively. Single-edge notched (SEN) specimens, as shown in Fig. 1b, were used for the in situ tests. The thickness of the specimen and notch size were 2.8 mm and 0.35 mm, respectively. The specimens were loaded either in S–T or L–T orientations during in situ testing, where loading in S–T orientation implies that the direction of an applied load is parallel to the short-transverse (S) direction and the crack grows in the transverse direction (T), i.e., on L–T plane (Fig. 1b). SENT specimens were fatigue precracked before performing in situ experiments. Precracking was performed ex situ using a micro-force testing system (MTS Tytron 250 at Arizona State University). Nucleation of a crack from a notch is a time-consuming process that requires a higher load. Therefore, precracking was performed to obtain a sharp crack that can reduce the time for crack initiation/propagation while performing in situ studies. This helped in collecting enough information (or tomography scans as discussed in next paragraph) in the limited time available at Argonne National Laboratory to perform in situ experiments.

X-ray tomography was performed at the 2-BM beamline of the Advanced Photon Source at Argonne National Laboratory. The details of the tomography system at 2-BM have been provided elsewhere.<sup>32,33</sup> A scintillator screen (LuAG:Ce or CdWO<sub>4</sub>) was coupled with an objective lens and a camera to capture 2D x-ray images of the specimens. These 2D projections were captured at an angular interval of 0.125° across a 180° range and were reconstructed using algorithms, such as a Gridrec Fast Fourier Transform (FFT)-based algorithm or filtered back-projection (FBP) reconstruction algorithm, to obtain 3D reconstruction.<sup>9</sup> The grayscale images obtained after reconstruction were analyzed, segmented, and quantified using ImageJ (ImageJ, Bethesda, MD), Matlab and Avizo® Fire (VSG, Burlington, MA). Three-dimensional rendering was performed using Mimics (Materialise, Ann Arbor, MI) and Avizo Fire (VSG, Burlington, MA) software.

### In Situ Loading Stage for Corrosive Environments

In situ experiments require a specialized loading stage to perform mechanical testing. Figure 2 shows the loading stage for testing in air.<sup>34</sup> The stage has a stepper motor coupled with a linear actuator (stroke length of 25 mm), a 500-N capacity load cell, a top grip attached to the actuator, and a bottom grip attached to the load cell. As a result of the weight limit of the motion stage at the 2BM beamline, the weight of the mechanical testing stage was restricted to 2 kg. The specimen was loaded from the top and clamped between the top and bottom grips, as shown in Fig. 2. Being transparent to

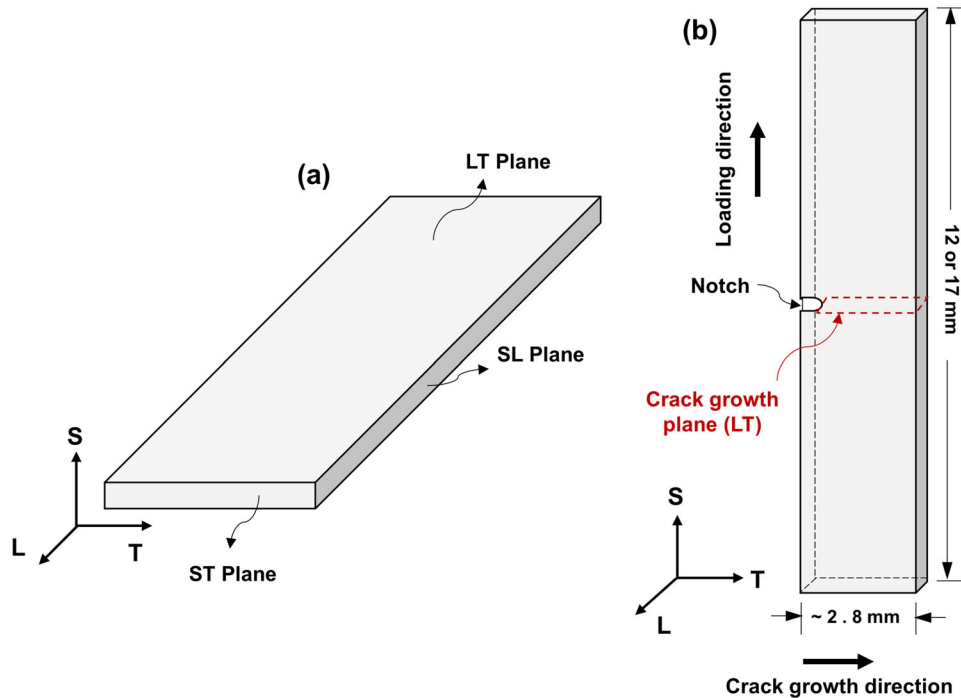


Fig. 1. (a) Schematic of a rolled Al 7075 plate shows all directions (L, T, S) and planes (L–T, S–T, S–L) and (b) schematic of a single edge notched (SEN) specimen to perform in situ experiments. The loading direction, crack growth direction, and crack growth plane have been shown in (b) when the specimen is loaded in S–T orientation.

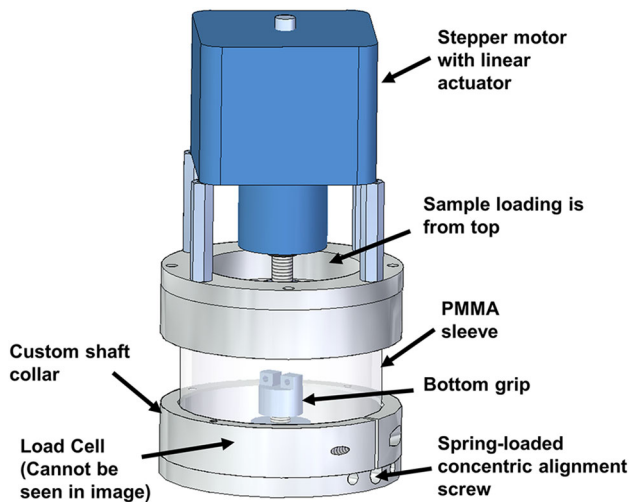


Fig. 2. In situ loading stage, showing all components, to conduct mechanical testing in air.<sup>34</sup> Load cell is at the bottom of the stage, and displacement is applied through the motor.

x-rays, a PMMA (Poly methyl methacrylate) sleeve was used to transmit the load from the top to the bottom of the stage. The loading stage must have provisions for specimen alignment to reduce the contribution from bending during uniaxial loading. Concentric alignment was done by translating the top grip relative to the bottom grip using set screws. Shims were used to minimize the axial misalignment. The top grip was also allowed to rotate freely

about its mounting screw to self-align in the third rotational direction. It should be noted here that the philosophy of loading stage design has remained same over the years. In other studies,<sup>26–28</sup> a load cell has also been used to measure the load, a motor to apply displacement, and x-ray transparent sleeve (PMMA) to transfer the load from the top of the stage to the bottom. Yet, the size and specifications of the loading stage were different. For example, the capacity of the load cell in the study of Babout et al.<sup>26</sup> was 5 kN as compared with 500 N in this study.

To perform in situ testing in corrosive media, modifications were incorporated into the original loading stage (Fig. 2). The mechanical testing stage (or loading stage) to perform tests in moisture is shown in Fig. 3a.<sup>35</sup> An annular wet sponge was placed at the bottom of the loading stage for continuous supply of moisture. A plastic wrap was used to cover the top opening of the stage to minimize moisture escape and maximize the relative humidity (R.H.). A humidity sensor was also placed inside the loading stage to measure the temperate and relative humidity throughout the experiment. The specimen was clamped between the top and bottom grips.

Modifications in the original loading stage (Fig. 2) to perform experiments in the liquid environment are shown in Fig. 3b.<sup>36</sup> The bottom steel grip was replaced with PEEK (Polyether ether ketone) as it is chemically inert to many solutions and exhibits sufficient strength. To accommodate the specimen, a

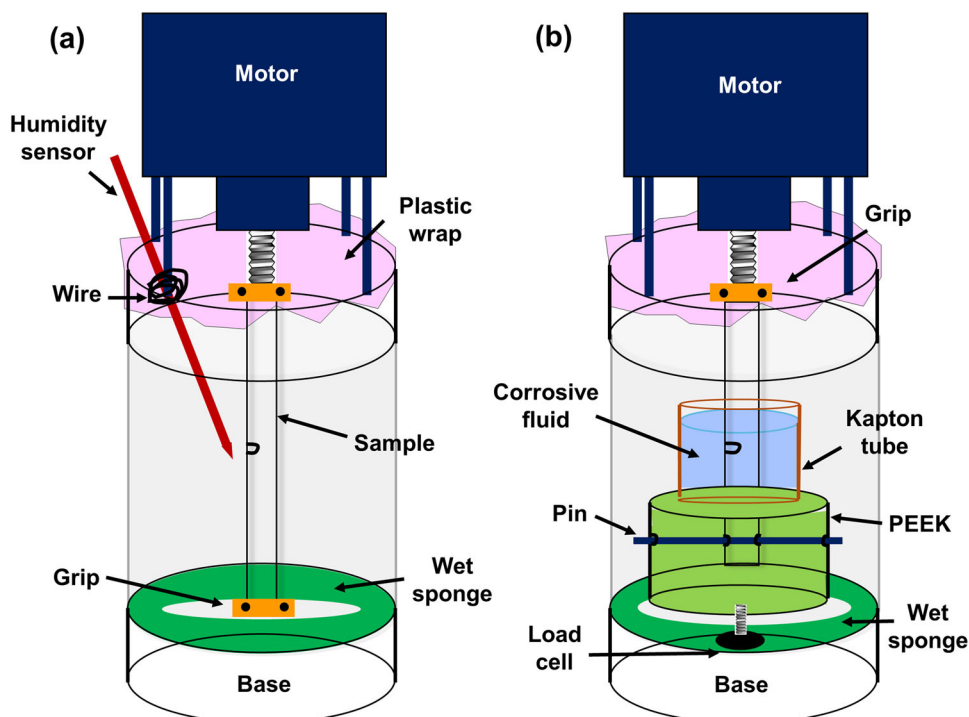


Fig. 3. Interior modification in the original loading stage (Fig. 2) to perform in situ experiments in corrosive environments (a) in moisture<sup>35</sup> and (b) in liquid environment.<sup>36</sup> Note that the bottom steel grip in (a) was replaced by PEEK in (b) to accommodate the liquid environment in the latter.

rectangular hole was made on the top of the cylindrical PEEK grip. Furthermore, to accommodate the stainless steel, a circular hole was made on the side wall of the cylindrical PEEK grip. It is to be noted here that the steel pin also passes through the hole made in the specimen. Epoxy was then added to increase the strength and permanence of the connection between the sample and the grip. Although the bottom was pin loaded, the top part of the sample was clamped in the top steel grip (similar to the moisture case). To hold the corrosive fluid, a Kapton tube (also chemically inert to many solutions) was attached to the PEEK cylinder with epoxy.

## RESULTS AND DISCUSSION

### In Situ Stress Corrosion Cracking of Al 7075 Alloys

#### *In Situ SCC in Moisture*

The arrangements in the loading stage, as shown in Fig. 3a, provided a constant relative humidity of ~95–96%.<sup>35</sup> In situ SCC experiments were performed in moisture to understand the crack growth behavior of Al 7075 alloys in three dimensions. The energy of the monochromatic x-ray beam was ~24 keV. Figure 4 shows the 3D rendering of stress corrosion cracks with time at a constant load of 110 N. Note that the time here represents that cumulative time of stress corrosion cracking. By using x-ray synchrotron tomography, it was possible

to detect two independent cracks that would not have been possible to observe by conventional 2D techniques. Furthermore, significant variations in the crack length were observed through thickness, asserting the need for 3D measurement techniques over 2D characterization. In general, the crack growth behavior during fatigue (in air) has been observed to vary from the surface to the interior of the specimen. The crack length is always larger in the interior than on the surface as a result of the plane stress condition in the latter.<sup>12</sup> Yet, the crack growth behavior during SCC becomes more nonuniform, especially when the crack growth is intergranular in nature, i.e., through grain boundaries. The SCC crack growth in aluminum alloys has been thought to be intergranular in nature and therefore crack bridging (“Introduction” section), formation of discontinuous cracks (discussed in next paragraph), etc. take place, leading to a highly nonuniform crack growth.

Interestingly, discontinuous cracks were observed on both sides of the specimen, as shown in Fig. 5. These 2D images were obtained from x-ray synchrotron tomography after 25 h of stress corrosion cracking. These discontinuous surface cracks have also been observed in Al alloys<sup>37</sup> and steel.<sup>38</sup> It was suggested that surface cracks nucleate in front of the main crack, grow separately, and then combine with the main crack.<sup>36,37</sup> Here, surface cracks represent the cracks on the surface of the specimen; i.e., surface crack length will indicate the length of the crack on the surfaces (sides) of the specimen.

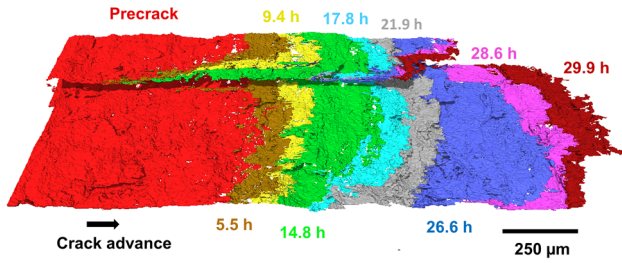


Fig. 4. 3D SCC crack profile of Al 7075, in moisture, as a function of time. Note that there are two independent cracks and crack length is highly nonuniform through the thickness.<sup>35</sup> The time here is the cumulative time during SCC.

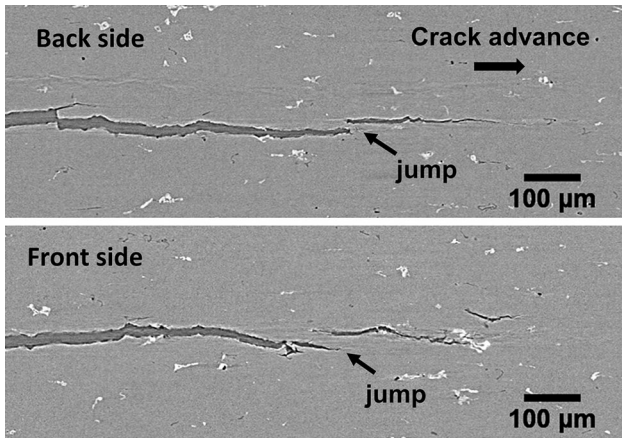


Fig. 5. 2D x-ray tomography images show discontinuous cracks on both surfaces (parallel to S-T plane) of the sample.<sup>35</sup>

Figure 6a through f shows the formation of one discontinuous surface crack and further growth in 3D. Figure 6a through d shows the side view of the crack, whereas Fig. 6e and f provides the top view of Fig. 6a and b, respectively. These 3D renderings with time (in the legend) show that these discontinuous surface cracks are connected in 3D. It is evident that the main crack grew from inside (Fig. 6a and b) and finally appeared as a discontinuous and separate crack on the surface. The appearance of the discontinuous crack can clearly be seen at 17.8 h (Fig. 6e) and 19.9 h (Fig. 6f) of SCC crack growth. The formation of these discontinuous cracks might be attributed to the intergranular crack growth behavior of Al 7075 alloys as the vertical distances between the surface cracks on both surfaces (Fig. 5) is approximately the same as the grain size along the S direction.

The 2D and 3D crack growth rates were measured and compared (Fig. 7). The crack growth rates were measured using the average crack lengths through thickness (3D measurement) and average of the crack lengths of both surfaces (2D measurement). The standard process of obtaining crack growth data in 2D is to measure crack lengths on the surfaces; therefore, we have followed the same while dealing with 2D measurements. The calculated crack growth rates in 2D showed significant variability than the calculated 3D growth rates using the average crack length through the thickness. Moreover, the deviations in 2D surface crack lengths led to significant differences in the stress intensity factors, as demonstrated by the error bars

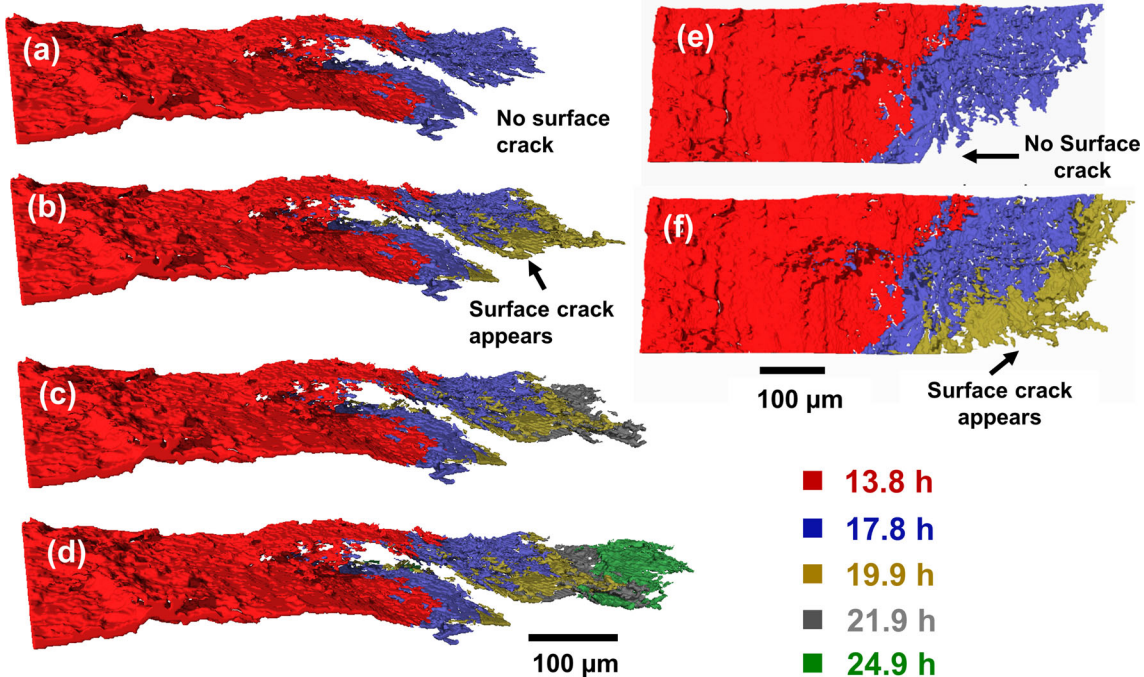


Fig. 6. 3D rendering of SCC crack shows the appearance of discontinuous crack on the surface and further growth (a–d: side view, e–f: top view). Crack appears on the surface in (b) and then continues to grow (c–d). The top views of (a) and (b) are shown in (e) and (d), respectively.<sup>35</sup>

in Fig. 7. In the case of 2D (filled blue circles), the stress intensity factor value is calculated by using the average crack length of the two surface crack lengths. The error bar is the difference between the two stress intensity factors (or the range of stress intensity factor) calculated from the two surface crack lengths. The calculation of a stress intensity factor for SEN specimen was performed using the equations proposed by Ahmed et al.<sup>39</sup> The large difference in the surface crack lengths can be attributed to the highly nonuniform growth of the SCC crack that includes formation of discontinuous cracks and independent growth of the two cracks. The results obtained here show the necessity of 3D

techniques, such as x-ray synchrotron tomography, to study the crack growth behavior during stress corrosion cracking.

*In Situ SCC of Al 7075 in Deionized Water*

To understand the SCC behavior of Al 7075 alloys in deionized water, in situ experiments were performed using the arrangements shown in Fig. 3b.<sup>36</sup> A constant load of 130 N was applied on an underaged Al 7075 specimen in S-T orientation (Fig. 1b). A pink beam, with an energy range of 15–31 keV, was used in place of the conventional monochromatic beam used earlier. The pink beam provides a higher photon flux than does a monochromatic beam. Therefore, the use of a pink beam resulted in faster data acquisition, i.e., more number of scans, leading to more information on the progression of corrosion. Although use of a monochromatic beam results in a scanning time of 20 min, the scanning time in the pink beam is a few seconds.<sup>34</sup>

It should be noted here that the crack did not grow for the initial 12 h after the start of SCC. Therefore, the specimen was again precracked in situ in DIUF (deionized ultra-filtered) water at Argonne National Laboratory to grow the crack further (obtain a sharp crack). This was followed by SCC at a constant load of 130 N. Figure 8 shows the minimum Z-projection of a 3D volume when looking into the crack growth plane (L-T plane) after ~56 min of stress corrosion cracking in deionized ultra-filtered (DIUF) water.<sup>36</sup> The 3D volume was obtained after reconstruction of the obtained 2D images during scan, as mentioned earlier. In addition to the notch, precracked, and SCC regions, hydrogen bubbles can also be observed on both surfaces of the specimen. As tomography scans were taken frequently, the crack profile was known before and after in situ precracking, leading to demarcation of these regions, as shown in Fig. 8.

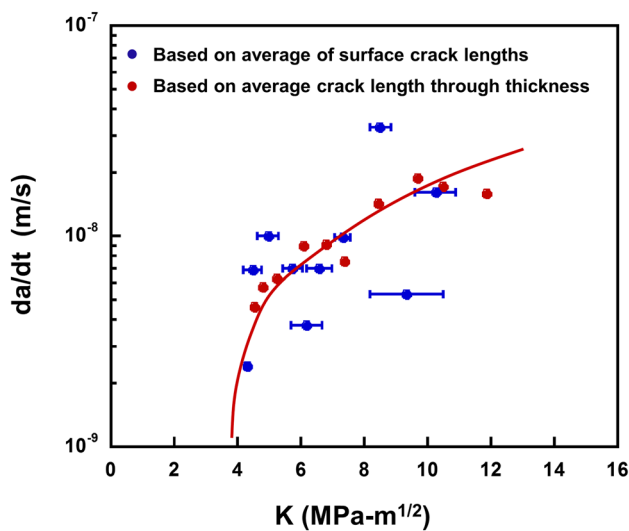


Fig. 7. Comparison of SCC crack growth rates based on 2D and 3D measurements. 2D measurement includes crack lengths on both sides of the specimen, whereas 3D measurement includes crack length through the thickness of the specimen. 3D crack growth rate measurement is uniform.<sup>35</sup>

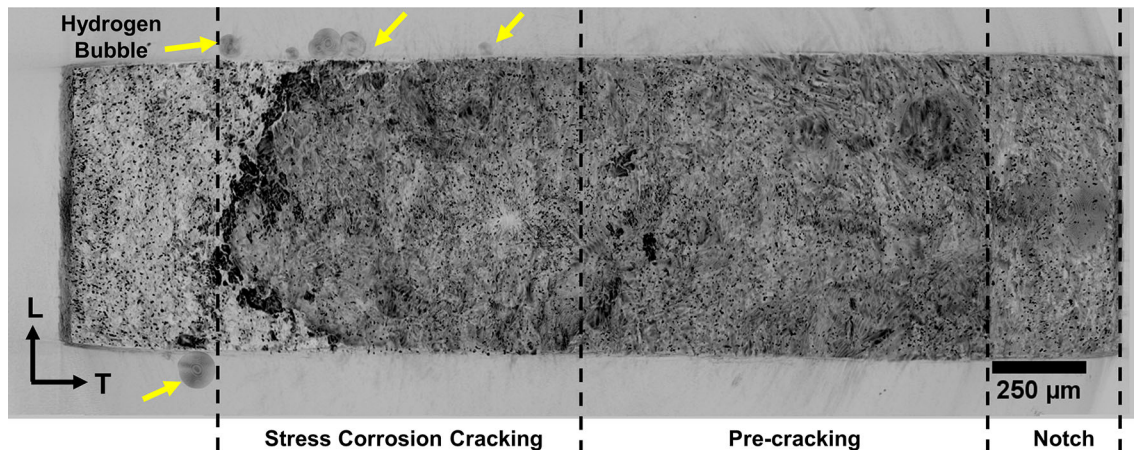


Fig. 8. Minimum Z-projection of a 3D volume after 56 min of SCC.<sup>36</sup> The Z-projection shows notch, SCC, and precracked regions and hydrogen bubbles. Note that loading was done in S direction, and therefore, the crack growth plane is L-T (Fig. 1b).

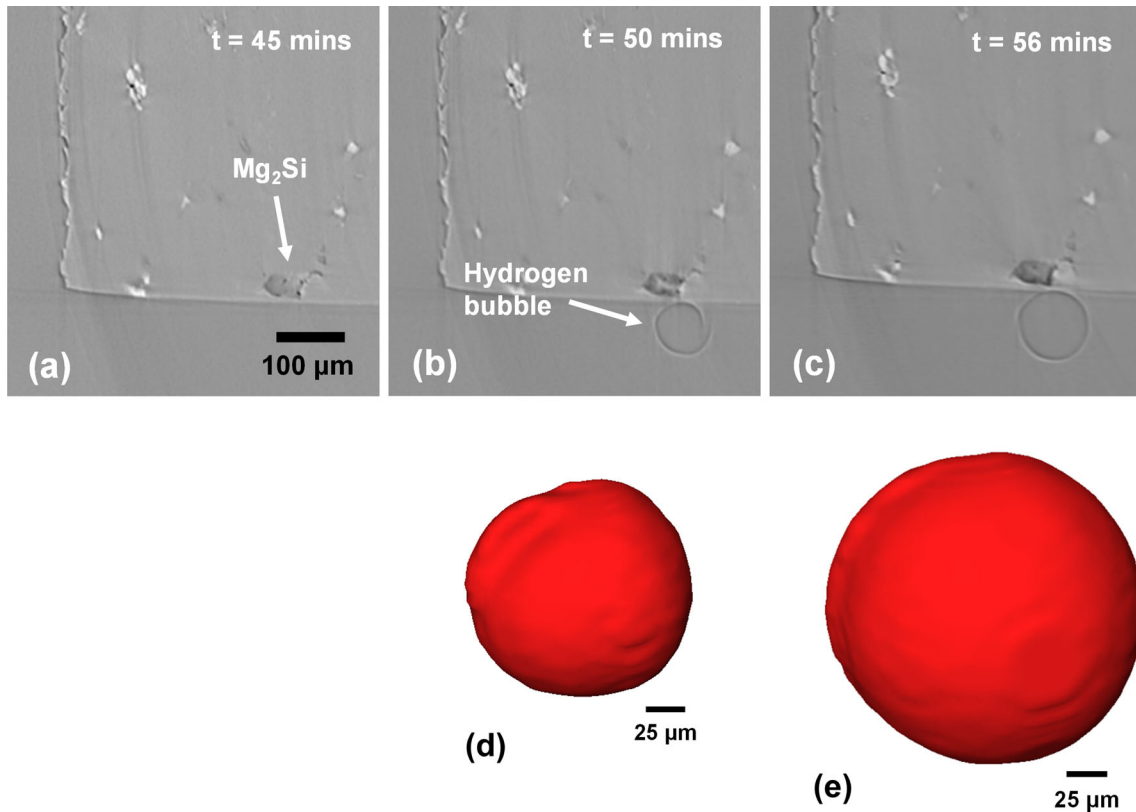


Fig. 9. (a–c) Hydrogen bubble evolution with time as corrosion of  $Mg_2Si$  inclusion progresses. Hydrogen bubble generates as a result of cathodic reactions, and the volume of this bubble increases as dissolution of  $Mg_2Si$  progresses. 3D rendering of the corresponding hydrogen bubble at (d) 50 min and (e) 56 min.<sup>36</sup>

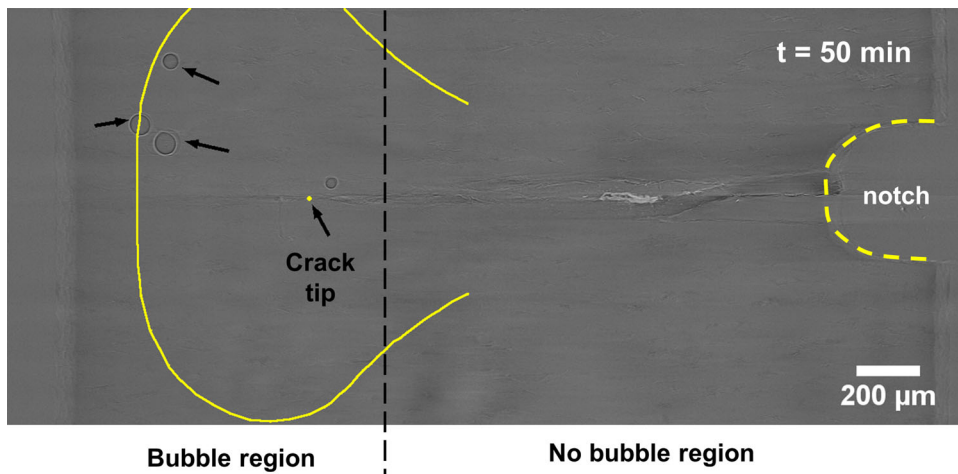


Fig. 10. Plastic zone contour (solid yellow) shows that  $Mg_2Si$  inclusions producing hydrogen bubbles are within the plastic zone, indicating the effect of stress on the formation of hydrogen bubbles from  $Mg_2Si$  inclusions during SCC.<sup>36</sup> Notch is also shown with a dotted yellow line (Color figure online).

Many of these surface hydrogen bubbles were found to be in close proximity to  $Mg_2Si$  particles, which are generally present in aluminum alloys as second-phase inclusion particles.<sup>31,40</sup> It has been shown that these inclusions are more anodic than the matrix in acidic and neutral media; i.e., they

form galvanic couples with the aluminum matrix.<sup>41</sup> These  $Mg_2Si$  inclusions tend to dissolve into the solution (anodic reaction), resulting in the evolution of hydrogen bubbles resulting from cathodic reactions.<sup>41–43</sup> It has also been proposed by several authors that magnesium selectively dissolves into

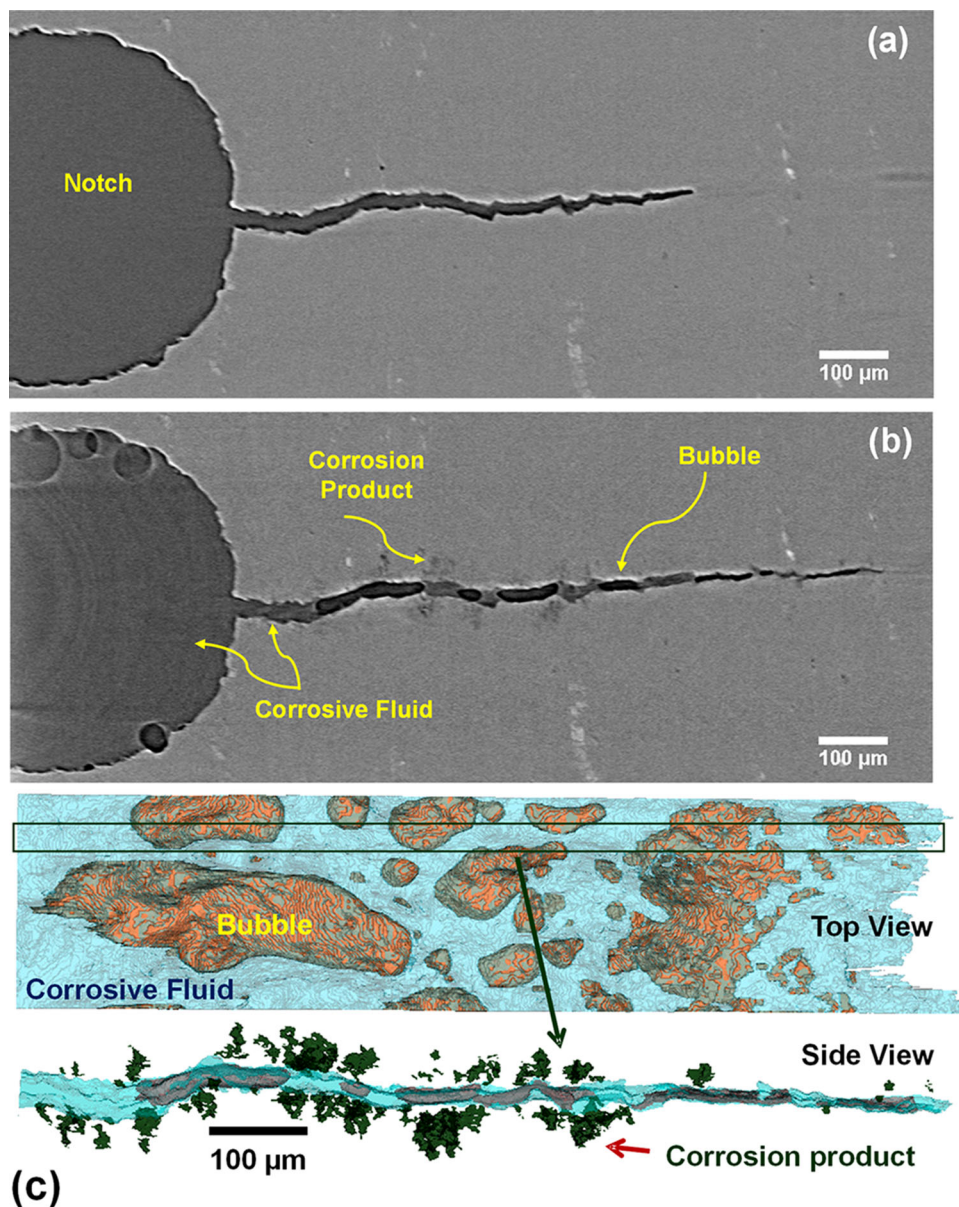


Fig. 11. 2D x-ray tomography images (a) before addition of EXCO solution and (b) after corrosion fatigue in the presence of EXCO solution. Note that notch, hydrogen bubbles, corrosion product, and corrosive fluid (EXCO solution) have been shown. (c) 3D renderings of a fatigue crack (fluid + bubble) and corrosion products. Note that the rendering of corrosion products is from a selected area.<sup>29</sup>

the solution (dealloying process) leaving behind Si-rich particles.<sup>43</sup> As a result of the slightly acidic nature of DIUF water (pH  $\sim$  5.5) and absence of other ions, we believe that hydrogen evolution is the result of cathodic reaction.

Figures 9a through c shows the progress of corrosion of  $Mg_2Si$  along with the evolution of a hydrogen bubble with time. The three-dimensional renderings of the same hydrogen bubble at 50 min and 56 min of SCC are shown in Fig. 9d and e, respectively. As 1 mol of hydrogen gas is produced by 1 mol of magnesium, the change in volume of hydrogen bubble (from 50 min to 56 min) can be used to calculate the corrosion rate of  $Mg_2Si$  inclusions. Two  $Mg_2Si$  inclusions on the surface, where

hydrogen bubbles did not move with time, were selected for the purpose of calculation of the corrosion rate. The calculated corrosion rates of the  $Mg_2Si$  inclusions were found to be  $\sim 2.55 \times 10^2$  g/m<sup>2</sup> days and  $3.68 \times 10^2$  g/m<sup>2</sup> days. These results indicate that x-ray synchrotron tomography can be used to measure the localized corrosion rates.

In aluminum alloys, halide (chloride) ions are required to break the passive film, resulting in pitting corrosion.<sup>44</sup> Interestingly, pitting corrosion occurred in the absence (or negligible) of chloride ions in DIUF water during the SCC experiment. This might be attributed to the effect of stress that contributed to the formation of a fresh-cracked  $Mg_2Si$  particle or debonded surface, leading to the



initiation of corrosion. The role of stress on pitting corrosion is shown in Fig. 10, which is a 2D slice approximately  $8.8 \mu\text{m}$  away from one of the two sides of the specimen (parallel to the S–T plane). It should be mentioned here that the tomography scans did not show any bubble in the first 12 h of SCC before in situ fatigue precracking was performed. Additionally, no bubbles were observed near  $\text{Mg}_2\text{Si}$  inclusions even after 40 min of stress corrosion cracking.<sup>36</sup> As these surface bubbles appeared only after 40 min of SCC, we can conclude that these are not trapped air bubbles (while

pouring deionized water in the Kapton tube) but are hydrogen bubbles generated as a result of the cathodic process during corrosion. As the crack grew longer, hydrogen bubbles were only observed near the crack tip region (labeled as “bubble region”) and not near the notch/precracked region (marked as “no bubble region”). The other side of the specimen showed the same trend where bubbles also appeared only in front of the crack tip. This behavior might be attributed to the higher stress intensity factor at the crack tip, which resulted in the fracture of particles or debonded surface. To substantiate this hypothesis, a plastic zone was calculated at the crack tip in the plane stress condition and then overlaid (sold yellow contour) on the 2D x-ray tomography image (Fig. 10). It should be mentioned here that the plastic zone size is twice the radius of yielding and the calculation was based on the mode I crack opening and von Mises yield criterion.<sup>45</sup> It is evident from Fig. 10 that  $\text{Mg}_2\text{Si}$  particles producing hydrogen bubbles were well within the calculated plastic zone. This supports our hypothesis that stress is important in driving corrosion of  $\text{Mg}_2\text{Si}$  particles in the absence of halide ions.

#### In Situ Corrosion-Fatigue of Al 7075 Alloys

In situ corrosion-fatigue experiments were performed on Al 7075-T651 using the arrangements shown in Fig. 3b.<sup>29,34</sup> An EXCO solution (4 M NaCl, 0.5 M  $\text{KNO}_3$  and 0.1 M  $\text{HNO}_3$ ) was used as a corrosive medium to ensure a significant amount of corrosion in the limited time available at the synchrotron beamline. EXCO is used as a standard solution to assess the exfoliation corrosion susceptibility of aluminum alloys.<sup>46</sup> The sample was loaded in L–T orientation; i.e., the loading direction, crack growth direction and crack growth plane were L, T, and S–T, respectively. Fatigue experiments

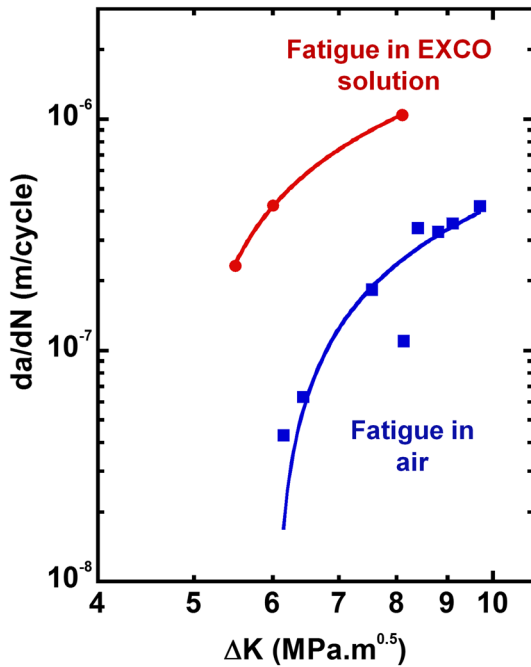


Fig. 12. Fatigue crack growth rates with and without EXCO solution. Crack growth rate is higher in the presence of a corrosive environment.

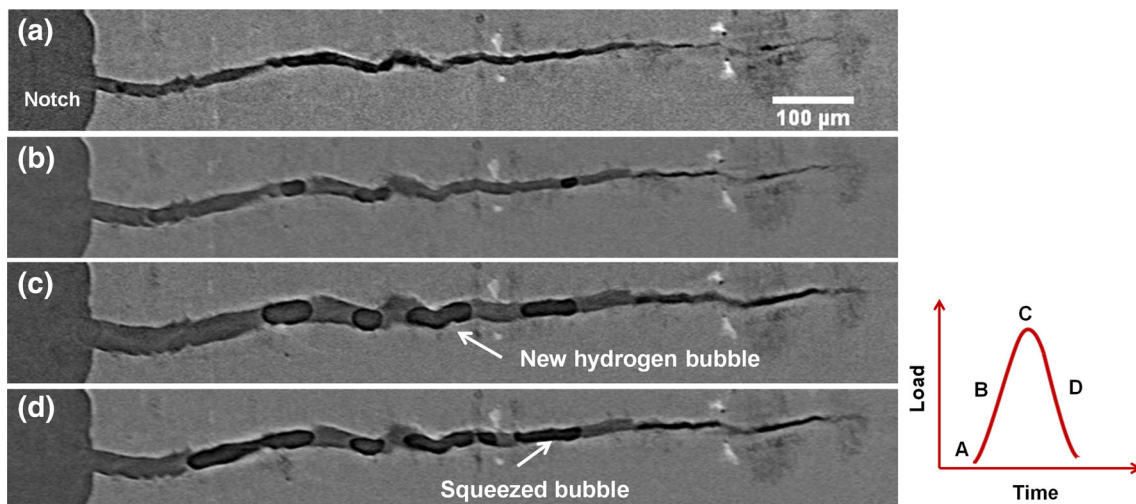


Fig. 13. 2D x-ray tomography images show changes in the morphology of hydrogen bubbles and formation of a new hydrogen bubble during a fatigue cycle (right figure).<sup>29,34</sup>

were conducted in the Paris law regime at a frequency of 0.5 Hz and R-ratio of 0.1. A pink beam was used for the advantages discussed earlier.

Figure 11a and b represents 2D x-ray synchrotron tomography images before and after fatigue corrosion (after 142 min of addition of solution), respectively. Hydrogen bubbles inside a fatigue crack, corrosion product (formed as a result of a reaction between Al 7075 and EXCO solution), and corrosive fluid (EXCO solution) can be observed in Fig. 11b, which were not present in Fig. 11a. Peak-aged Al 7xxx alloys have been shown to be highly susceptible to exfoliation corrosion.<sup>47–49</sup> The corrosion products have been thought to be  $\text{Al}(\text{OH})_3$ , and hydrogen bubbles are produced as a result of cathodic reaction.<sup>29,48–50</sup> Figure 11c shows the corresponding 3D rendering of the fatigue crack, hydrogen bubbles, corrosive fluid, and corrosion products. It is to be noted that segmentation of corrosion products was performed only on a few slices, i.e., only from a part of crack. The hydrogen bubbles occupied approximately 32% of the overall volume of the fatigue crack.

Figure 12 shows the measured fatigue crack growth rates with and without the EXCO solution, where it is evident that the presence of corrosive medium accelerated the crack growth rate. Recently, Maralund et al.<sup>48,49</sup> proposed that exfoliation corrosion in aluminum alloys can occur via intergranular dissolution-induced damage (IDD) or intergranular fracture-induced damage (IFD) or a combination of these two mechanisms. These mechanisms along with fatigue damage led to higher crack growth rates of Al 7075 alloys in EXCO solution than in air.

Figure 13 shows the changes in the morphology of hydrogen bubbles and formation of a new hydrogen bubble (inside a fatigue crack) during a fatigue cycle. This new hydrogen bubble can be observed at position C that was not present in position B. All bubbles were squeezed as the crack closed during unloading (position D). These results provide insights into the fundamentals of evolution of hydrogen bubbles inside a growing fatigue crack that would not have been possible with conventional 2D measurement techniques.

## SUMMARY

We have described our recent in situ experiments to show the importance and necessity of x-ray tomography in the investigation of stress corrosion cracking and corrosion fatigue. By using x-ray synchrotron tomography, we have been able to show that discontinuous surface cracks in SCC are a single continuous and tortuous crack in three dimensions (3D). Crack growth rates obtained from 3D measurement have been found to be more realistic than crack growth rates obtained from 2D techniques. During SCC of Al7075 alloys, it was shown that stress is necessary to initiate the pitting

corrosion of  $\text{Mg}_2\text{Si}$  particles in DIUF water. During fatigue in EXCO solution, the morphology of hydrogen bubbles inside the crack changed during a fatigue cycle along with the formation of a new hydrogen bubble. These results would not have been attainable through conventional two-dimensional techniques and require a three-dimensional technique such as x-ray tomography.

## ACKNOWLEDGEMENTS

The authors are grateful for the financial support from the Office of Naval Research (ONR) under Contract Number N000141010350 (Drs. W. Mullins and A.K. Vasudevan, Program Managers).

## REFERENCES

1. S.R. Stock, *Characterization of Materials* (Wiley, 2012), pp. 1–18.
2. J.J. Williams, N.C. Chapman, V. Jakkali, V.A. Tanna, N. Chawla, X. Xiao, and F. De Carlo, *Metall. Mater. Trans. A* 42A, 2999 (2011).
3. S.R. Stock, *Microcomputed Tomography: Methodology and Applications* (Boca Raton: CRC Press, 2008).
4. S.R. Stock, *Int. Mater. Rev.* 53, 129 (2008).
5. J.C.E. Mertens, J.J. Williams, and N. Chawla, *Mater. Charact.* 92, 36 (2014).
6. L. Salvo, M. Suery, A. Marmottant, N. Limodin, and D. Bernard, *C. R. Phys.* 11, 641 (2010).
7. E. Maire, J.-Y. Buffiere, L. Salvo, J.J. Blandin, W. Ludwig, and J.M. Letang, *Adv. Eng. Mater.* 3, 539 (2001).
8. J.C.E. Mertens, J.J. Williams, and N. Chawla, *J. Electron. Mater.* 43, 4442 (2014).
9. J. Baruchel, J.-Y. Buffiere, E. Maire, P. Merle, and G. Peix, *X-Ray Tomography in Material Science* (Paris: HERMES Science Publications, 2000).
10. F.A. Silva, J.J. Williams, B.R. Mueller, M.P. Hentschel, P.D. Portella, and N. Chawla, *Metall. Mater. Trans. A* 41A, 2121 (2010).
11. E. Maire and P.J. Withers, *Int. Mater. Rev.* 59, 1 (2014).
12. J.J. Williams, K.E. Yazzie, E. Padilla, N. Chawla, X. Xiao, and F. De Carlo, *Int. J. Fatigue* 57, 79 (2013).
13. P.J. Withers and M. Preuss, *Ann. Rev. Mater. Res.* 42, 81 (2012).
14. J.-Y. Buffiere, E. Maire, J. Adrien, J.P. Masse, and E. Boller, *Exp. Mech.* 50, 289 (2010).
15. F. Beckmann, R. Grupp, A. Haibel, M. Huppmann, M. Nöthe, A. Pyzalla, W. Reimers, A. Schreyer, and R. Zettler, *Adv. Eng. Mater.* 9, 939 (2007).
16. B.M. Patterson, N.L. Cordes, K. Henderson, J.J. Williams, T. Stannard, S.S. Singh, A.R. Ovejero, X. Xiao, M. Robinson, and N. Chawla, *J. Mater. Sci.* 51, 171 (2016).
17. N.L. Cordes, K. Henderson, T. Stannard, J.J. Williams, X. Xiao, M.W.C. Robinson, T.A. Schaedler, N. Chawla, and B.M. Patterson, *Microsc. Today* 23, 12 (2015).
18. E. Maire, S.X. Zhou, J. Adrien, and M. Dimichiel, *Eng. Fract. Mech.* 78, 2679 (2011).
19. E. Maire, V. Carmona, J. Courbon, and W. Ludwig, *Acta Mater.* 55, 6806 (2007).
20. A. Isaac, F. Sket, W. Reimers, B. Camin, G. Sauthoff, and A.R. Pyzalla, *Mater. Sci. Eng. A* 478A, 108 (2008).
21. A. Guvenilir, T.M. Breunig, J.H. Kinney, and S.R. Stock, *Acta Mater.* 45, 1977 (1997).
22. N.C. Chapman, J. Silva, J.J. Williams, N. Chawla, and X. Xiao, *Mater. Sci. Technol.* 31, 573 (2014).
23. K.H. Khor, J.-Y. Buffiere, W. Ludwig, H. Toda, H.S. Ubhi, P.J. Gregson, and I. Sinclair, *J. Phys. Condens. Mater.* 16, S3511 (2004).
24. H. Toda, I. Sinclair, J.-Y. Buffiere, E. Maire, T. Connolly, M. Joyce, K.H. Khor, and P. Gregson, *Philos. Mag.* 83, 2429 (2003).
25. P. Hrubby, S.S. Singh, J.J. Williams, X. Xiao, F. De Carlo, and N. Chawla, *Int. J. Fatigue* 68, 136 (2014).

26. L. Babout, T.J. Marrow, D. Engelberg, and P.J. Withers, *Mater. Sci. Technol.* 22, 1068 (2006).
27. T.J. Marrow, L. Babout, A.P. Jivkov, P. Wood, D. Engelberg, N. Stevens, P.J. Withers, and R.C. Newman, *J. Nucl. Mater.* 352, 62 (2006).
28. A. King, G. Johnson, D. Engelberg, W. Ludwig, and T.J. Marrow, *Science* 321, 382 (2008).
29. S.S. Singh, J.J. Williams, X. Xiao, F. De Carlo, and N. Chawla, *Fatigue of Materials II: Advances and Emergences in Understanding*, ed. T.S. Srivatsan, A.M. Imam, and R. Srinivasan (Pittsburgh: Materials Science and Technology, 2012), .
30. S.S. Singh, E. Guo, H. Xie, and N. Chawla, *Intermetallics* 62, 69 (2015).
31. S.S. Singh, J.J. Loza, A.P. Merkle, and N. Chawla, *Mater. Charact.* 118, 102 (2016).
32. J.J. Williams, Z. Flom, A.A. Amell, N. Chawla, X. Xiao, and F. De Carlo, *Acta Mater.* 58, 6194 (2010).
33. S.S. Singh, C. Schwartzstein, J.J. Williams, X. Xiao, F. De Carlo, and N. Chawla, *J. Alloys Compd.* 602, 163 (2014).
34. S.S. Singh, J.J. Williams, P. Hruby, X. Xiao, F. De Carlo, and N. Chawla, *Integr. Mater. Manuf. Innov.* 3, 1 (2014).
35. S.S. Singh, J.J. Williams, M.F. Lin, X. Xiao, F. De Carlo, and N. Chawla, *Mater. Res. Lett.* 2, 217 (2014).
36. S.S. Singh, J.J. Williams, T.J. Stannard, X. Xiao, F. De Carlo, and N. Chawla, *Corros. Sci.* 104, 330 (2016).
37. J. Zhang, S. Kalnaus, M. Behrooz, and Y. Jiang, *Metall. Mater. Trans. A* 42, 448 (2011).
38. L.J. Qiao, K.W. Gao, A.A. Volinsky, and X.Y. Li, *Corros. Sci.* 53, 3509 (2011).
39. J. Ahmad, V. Papaspyropoulos, and A.T. Hopper, *Eng. Fract. Mech.* 38, 283 (1991).
40. A.P. Merkle, L. Lechner, A. Steinbach, J. Gelb, M. Kienle, M.W. Phaneuf, D. Unrau, S.S. Singh, and N. Chawla, *Microsc. Microanal.* 28, S10 (2014).
41. N. Birbilis and R.G. Buchheit, *J. Electrochem. Soc.* 155, C117 (2008).
42. R.K. Gupta, N.L. Sukiman, K.M. Fleming, M.A. Gibson, and N. Birbilis, *ECS Electrochem. Lett.* 1, C1 (2012).
43. E. Linardi, R. Haddad, and L. Lanzani, *Proc. Mater. Sci.* 1, 550 (2012).
44. S. Ghosh (Ph.D. Dissertation, University of Birmingham, 2008).
45. T.L. Anderson, *Fracture Mechanics: Fundamentals and Applications*, 3rd ed. (Boca Raton: CRC Press, 2005).
46. ASTM G34: *Standard Test Method for Exfoliation Corrosion Susceptibility in 2XXX and 7XXX Series Aluminum Alloys (EXCO Test)*.
47. J. Wloka, T. Hack, and S. Virtanen, *Corros. Sci.* 49, 1437 (2007).
48. T. Marlaud, B. Malki, C. Henon, A. Deschamps, and B. Baroux, *Corros. Sci.* 53, 3139 (2011).
49. T. Marlaud, B. Malki, A. Deschamps, and B. Baroux, *Corros. Sci.* 53, 1394 (2011).
50. C. Vargel, *Corrosion of Aluminum* (San Diego: Elsevier Inc, 2004).